Hydrodynamic screening near planar boundaries: Effects on semiflexible polymer dynamics

Yann von Hansen, Michael Hinczewski, and Roland R. Netz

Citation: The Journal of Chemical Physics **134**, 235102 (2011); doi: 10.1063/1.3593458
View online: http://dx.doi.org/10.1063/1.3593458
View Table of Contents: http://scitation.aip.org/content/aip/journal/jcp/134/23?ver=pdfcov
Published by the AIP Publishing

Hydrodynamic screening near planar boundaries: Effects on semiflexible polymer dynamics

Yann von Hansen,[1] Michael Hinczewski,[1,a)] and Roland R. Netz[2,b)]
[1]*Physics Department, Technical University Munich, 85748 Garching, Germany*
[2]*Fachbereich Physik, Freie Universität Berlin, Arnimallee 14, D-14195 Berlin, Germany*

(Received 25 January 2011; accepted 3 May 2011; published online 16 June 2011)

The influence of hydrodynamic screening near a surface on the dynamics of a single semiflexible polymer is studied by means of Brownian dynamics simulations and hydrodynamic mean field theory. The polymer motion is characterized in terms of the mean squared displacements of the end-monomers, the end-to-end vector, and the scalar end-to-end distance. In order to control hydrodynamic screening effects, the polymer is confined to a plane at a fixed separation from the wall. When gradually decreasing this separation, a crossover from Zimm-type towards Rouse (free-draining) polymer dynamics is induced. However, this crossover is rather slow and the free-draining limit is not completely reached—substantial deviations from Rouse-like dynamics are registered in both simulations and theory—even at distances of the polymer from the wall on the order of the monomer size. Remarkably, the effect of surface-induced screening of hydrodynamic interactions sensitively depends on the type of dynamic observable considered. For vectorial quantities such as the end-to-end vector, hydrodynamic interactions are important and therefore surface screening effects are sizeable. For a scalar quantity such as the end-to-end distance, on the other hand, hydrodynamic interactions are less important, but a pronounced dependence of dynamic scaling exponents on the persistence length to contour length ratio becomes noticeable. Our findings are discussed against the background of single-molecule experiments on f-actin [L. Le Goff *et al.*, Phys. Rev. Lett. **89**, 258101 (2002)]. © *2011 American Institute of Physics*. [doi:10.1063/1.3593458]

I. INTRODUCTION

Semiflexible polymers are of interest in various fields of science and technology due to their abundance in biological and synthetic systems. Examples of wide biological relevance include double-stranded DNA and cytoskeletal filaments, such as actin and microtubules. The theoretical interest in semiflexible polymer dynamics[1–7] has been spurred since the manipulation and observation of single polymer filaments has become feasible experimentally. Nowadays, a variety of refined experimental techniques allow to follow precisely and analyze conformation and dynamics of single polymers under all kinds of different environments, including confinement in nanotubes and nanoslits.[8,9] To give explicit examples, internal relaxation dynamics of f-actin were resolved by fluorescence videomicroscopy,[10] and end-monomer dynamics of dsDNA were investigated by fluorescence correlation spectroscopy.[11,12] Although polymers are often confined due to practical reasons in such experiments, hydrodynamic interactions (HI) are—if considered at all—generally included in existing theories[13] assuming a boundless fluid. Though the importance of HI was demonstrated in a range of simulation studies on force- and/or shear-driven filaments,[1–3,7,14,15] the question how the internal equilibrium dynamics of a polymer change, when nearby surfaces alter the HI between different parts of the polymer, has received little attention and the influence of surface-induced hydrodynamic screening on semiflexible polymer dynamics has thus remained elusive.

Within the present paper we focus on one single semiflexible polymer, which is confined to a layer at fixed separation from a planar hydrodynamic boundary at which a no-slip boundary condition is enforced; the strength of HI thus varies depending on the distance to the wall. Polymer dynamics are studied by means of Brownian hydrodynamics simulations and compared with a hydrodynamic mean field theory (MFT). Our study demonstrates the complexity of semiflexible polymer dynamics resulting from a subtle interplay of chain connectivity, internal bending and stretching stiffness as well as (screened) HI. We find the importance of HI to vary among the different dynamic observables considered: while the mean squared displacement (MSD) of vectorial quantities such as the end-monomer position or the end-to-end vector sensitively depends on the HI strength, this dependence is much less pronounced for the MSD of a scalar quantity, such as the end-to-end distance. In the scalar case, on the other hand, a pronounced dependence of dynamic scaling exponents on the ratio of the bending and stretching stiffnesses and on the ratio of contour and persistence lengths appears in the data, in qualitative agreement with our reanalysis of experimental data for the internal relaxation dynamics of f-actin.[10] Interestingly, for the MSDs of vectorial quantities the crossover from Zimm-type behavior in bulk to Rouse-type behavior at the hydrodynamic boundary is rather slow and the free-draining limit is not completely reached even when the polymer distance from the wall is on the order of the monomer

a)Present address: Institute for Physical Science and Technology, University of Maryland, College Park, Maryland 20742, USA.
b)Electronic mail: netz@ph.tum.de.

size. An interesting question in the future thus concerns the relevance of hydrodynamics for the dynamics of biopolymers *in vivo* with omnipresent confining surfaces and the crowded environment of cellular systems.[16]

The paper is organized as follows: The essentials of low Reynolds-number hydrodynamics near a planar surface, which are used in both simulations and theory, are shortly revisited in Sec. II. The Brownian hydrodynamics scheme is described in Sec. III A; for the theoretical description of semiflexible polymer dynamics a hydrodynamic mean field approach[4] is adapted to the present context, details of which are found in Sec. III B. The results of hydrodynamic simulations and of the theory are presented and discussed in Sec. IV; the main implications of our findings are exposed in Sec. V. Explicit expressions for the hydrodynamic interaction tensor used for simulation purposes and within the analytic theory are found in the Appendix.

II. HYDRODYNAMICS NEAR A PLANAR NO-SLIP BOUNDARY

We assume the planar hydrodynamic boundary being placed in the xy-plane at $z = 0$ of the coordinate system. The no-slip boundary condition at the wall implies that all components of the solvent flow field vanish at the boundary. The incompressible Stokes equation,

$$\nabla p(\boldsymbol{r}) - \eta \nabla^2 \boldsymbol{v}(\boldsymbol{r}) = \boldsymbol{f}(\boldsymbol{r}), \quad \nabla \cdot \boldsymbol{v}(\boldsymbol{r}) = 0, \tag{1}$$

relating pressure p, fluid velocity $\boldsymbol{v}$, and an external force field $\boldsymbol{f}$, can be solved using a standard Green's function technique. The solution satisfying the no-slip condition at $z = 0$, named the Blake tensor $\overleftrightarrow{\mu}^{\mathrm{B}}$, is derived using the method of images,[17]

$$\overleftrightarrow{\mu}^{\mathrm{B}}(\boldsymbol{r}, \boldsymbol{r}') = \overleftrightarrow{\mu}^{\mathrm{O}}(\boldsymbol{r}_{\mathrm{rel}}) - \overleftrightarrow{\mu}^{\mathrm{O}}(\boldsymbol{R}) + \overleftrightarrow{\mu}^{\mathrm{D}}(\boldsymbol{R}) - \overleftrightarrow{\mu}^{\mathrm{SD}}(\boldsymbol{R}), \tag{2}$$

where $\boldsymbol{r}' = (x', y', z')^{\mathrm{T}}$ is the position of the Stokeslet, the image Stokeslet has coordinates $\bar{\boldsymbol{r}}' = (x', y', -z')^{\mathrm{T}}$, and the vectors $\boldsymbol{r}_{\mathrm{rel}} \equiv \boldsymbol{r} - \boldsymbol{r}'$, and $\boldsymbol{R} \equiv \boldsymbol{r} - \bar{\boldsymbol{r}}'$ were defined. The Oseen tensor $\overleftrightarrow{\mu}^{\mathrm{O}}$, the Stokes doublet $\overleftrightarrow{\mu}^{\mathrm{D}}$, and the source doublet $\overleftrightarrow{\mu}^{\mathrm{SD}}$ are 3×3-tensors with entries

$$\overleftrightarrow{\mu}^{\mathrm{O}}(\boldsymbol{r})_{\alpha\beta} = \frac{1}{8\pi\eta r}\left(\delta_{\alpha\beta} + \frac{r_\alpha r_\beta}{r^2}\right), \quad \alpha, \beta \in \{x, y, z\}, \tag{3}$$

$$\overleftrightarrow{\mu}^{\mathrm{D}}(\boldsymbol{R})_{\alpha\beta} = \frac{2z'^2(1 - 2\delta_{\beta z})}{8\pi\eta}\left(\frac{\delta_{\alpha\beta}}{R^3} - \frac{3R_\alpha R_\beta}{R^5}\right), \tag{4}$$

$$\overleftrightarrow{\mu}^{\mathrm{SD}}(\boldsymbol{R})_{\alpha\beta} = \frac{2z'(1 - 2\delta_{\beta z})}{8\pi\eta} \times \left(\frac{\delta_{\alpha\beta} R_z}{R^3} - \frac{\delta_{\alpha z} R_\beta}{R^3} + \frac{\delta_{\beta z} R_\alpha}{R^3} - \frac{3R_\alpha R_\beta R_z}{R^5}\right), \tag{5}$$

where $r \equiv |\boldsymbol{r}|$ and $R \equiv |\boldsymbol{R}|$. The hydrodynamic entrainment effect of the motion of a finite sized sphere of radius a located at $\boldsymbol{r}'$ on another equal-sized sphere at $\boldsymbol{r}$ is approximated by a multipole expansion[18,19] to second order in the bead radius a,

$$\overleftrightarrow{\mu}^{\mathrm{RPB}}(\boldsymbol{r}, \boldsymbol{r}') \equiv \left(1 + \frac{a^2}{6}\nabla_{\boldsymbol{r}}^2 + \frac{a^2}{6}\nabla_{\boldsymbol{r}'}^2\right)\overleftrightarrow{\mu}^{\mathrm{B}}(\boldsymbol{r}, \boldsymbol{r}'), \tag{6}$$

which in analogy to the procedure in an unbounded fluid is called the Rotne-Prager level[20] of the Blake tensor. The approximate expression for the HI between finite sized spheres in Eq. (6) is used in both simulations and theory as detailed in Sec. III; the explicit entries of the tensor are found in the Appendix.

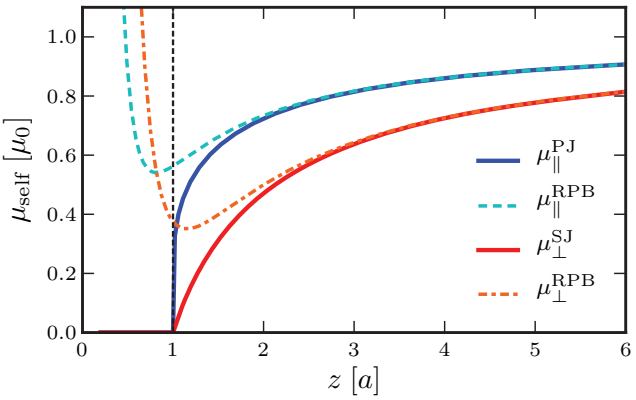

FIG. 1. Parallel ($\parallel$) and perpendicular ($\perp$) self-mobilities of a sphere of radius a located at a vertical distance z from a no-slip wall ($z = 0$). The approximations of Eqs. (8) and (9) (dashed lines) are compared to the result for the parallel mobility of Eq. (10) (solid blue line), and to the exact expression for the perpendicular mobility of Eq. (11) (solid red line). Self-mobilities are given in units of the bare self-mobility $\mu_0 = 1/(6\pi\eta a)$ in a fluid of viscosity η; the region $z < a$ is inaccessible due to excluded-volume effects.

A. Self-mobilities

The no-slip boundary at the wall not only alters HI between different particles, but also affects the particles' self-mobilities. Approximate expressions[18,19] for the dependence of the self-mobility of a sphere on the separation z to the wall are obtained by considering the limit,

$$\overleftrightarrow{\mu}_{\mathrm{self}}^{\mathrm{RPB}}(z) \equiv \lim_{\boldsymbol{r}\to\boldsymbol{r}'} \tilde{\overleftrightarrow{\mu}}^{\mathrm{RPB}}(\boldsymbol{r}, \boldsymbol{r}') = \begin{pmatrix} \mu_{\parallel}^{\mathrm{RPB}}(z) & 0 & 0 \\ 0 & \mu_{\parallel}^{\mathrm{RPB}}(z) & 0 \\ 0 & 0 & \mu_{\perp}^{\mathrm{RPB}}(z) \end{pmatrix}, \tag{7}$$

where $\tilde{\overleftrightarrow{\mu}}^{\mathrm{RPB}}$ is the Rotne-Prager level of the tensor $\tilde{\overleftrightarrow{\mu}}^{\mathrm{B}}$, in which—compared to the Blake tensor $\overleftrightarrow{\mu}^{\mathrm{B}}$ in Eq. (2)—the first Oseen contribution $\overleftrightarrow{\mu}^{\mathrm{O}}(\boldsymbol{r}, \boldsymbol{r}')$, which has a singularity at $\boldsymbol{r} = \boldsymbol{r}'$, is replaced by the diagonal 3×3 matrix $\mu_0 \overleftrightarrow{\mathbf{1}}$, $\mu_0 \equiv 1/(6\pi\eta a)$ being the bare Stokes self-mobility of a sphere of radius a in a solvent of viscosity η. One obtains renormalized self-mobilities parallel ($\parallel$) and perpendicular ($\perp$) to the boundary, which depend on the distance z from the wall,

$$\mu_{\parallel}^{\mathrm{RPB}}(z) = \mu_0\left(1 - \frac{9a}{16z} + \frac{1}{8}\left(\frac{a}{z}\right)^3\right) + \mathcal{O}(a^4), \tag{8}$$

$$\mu_{\perp}^{\mathrm{RPB}}(z) = \mu_0 \left(1 - \frac{9a}{8z} + \frac{1}{2}\left(\frac{a}{z}\right)^3\right) + \mathcal{O}(a^4). \quad (9)$$

In Fig. 1 the expressions in Eqs. (8) and (9), shown as broken lines, which only approximately fulfill the no-slip boundary condition on the bead's surface, are compared to more elaborate and experimentally tested results,[21] shown as solid lines, which correctly reproduce the short-range lubrication effects. The expression for the self-mobility parallel to the wall obtained by Perkins and Jones (PJ) (Ref. 22) and Stimson's and Jeffery's (SJ) exact result for the self-mobility perpendicular to the surface[23,24] read

$$\mu_{\parallel}^{\mathrm{PJ}}(z) = \mu_0 \Big(1 - \frac{8}{15}\log(1-\beta) + 0.029\beta + 0.04973\beta^2 - 0.1249\beta^3 + \ldots\Big)^{-1}, \quad \beta \equiv a/z, \quad (10)$$

$$\mu_{\perp}^{\mathrm{SJ}}(z) = \mu_0 \left(\frac{4}{3}\sinh\alpha \sum_{n=1}^{\infty} \frac{n(n+1)}{(2n-1)(2n+3)} \times \left[\frac{2\sinh((2n+1)\alpha) + (2n+1)\sinh(2\alpha)}{4\sinh^2((n+1/2)\alpha) - (2n+1)^2\sinh^2(\alpha)} - 1\right]\right)^{-1}, \quad \alpha \equiv \cosh^{-1}(z/a). \quad (11)$$

In Fig. 1, differences between the exact and the approximate self-mobilities are only noticeable for distances $z \lesssim 2a$. For the sake of consistency of self-mobilities and inter-bead HI described by the Rotne-Prager level of the Blake tensor [Eq. (6)], we resort to the approximate expressions in Eqs. (8) and (9) even for $z < 2a$. Since the continuum description of hydrodynamics is expected to break down in any case in the limit $z \to a$ — since single molecules have a non-vanishing mobility even when they are in direct contact with a surface— we do not attribute any experimental significance to the deviations between our approximate and the exact expressions in Fig. 1.

B. Hydrodynamic screening

HI are long-ranged, decaying as $1/r$ in an unbounded fluid; the term hydrodynamic screening is employed to describe the weakening of these HI, for example, in the presence of nearby surfaces. Within the following discussion, we restrict ourselves to the scenario schematically depicted in Fig. 2, two equal-sized spheres of radius a at a distance z from the no-slip interface and at a separation r from each other along the x axis of the coordinate frame. As illustrated in Fig. 2, the hydrodynamic flow-field created by a force $\boldsymbol{f}$ acting on one of the spheres also causes a motion with velocity $\boldsymbol{v} = \overleftrightarrow{\boldsymbol{\mu}}^{\mathrm{RPB}} \cdot \boldsymbol{f}$ of the other one. In the panels (a)–(c) of Fig. 3, the strengths of HI at different distances from the wall are compared: the diagonal entries of the Rotne-Prager level of the Blake tensor $\overleftrightarrow{\boldsymbol{\mu}}^{\mathrm{RPB}}$, specified in detail in the Appendix, are shown as a function of the interparticle distance r. While HI remain long-ranged decaying as $1/r$ for $r \ll z$, a crossover to a $1/r^3$-scaling is observed

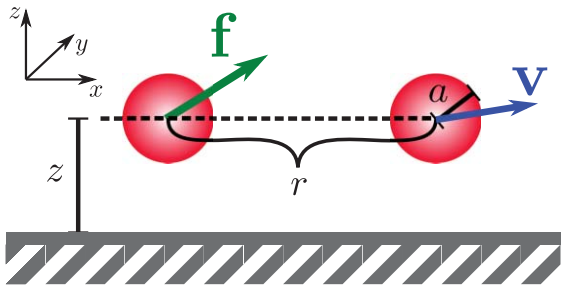

FIG. 2. Schematic illustration of the bead configuration for which the diagonal elements of the hydrodynamic interaction tensor relating the force $\boldsymbol{f}$ acting on one of the beads and the velocity $\boldsymbol{v}$ of the other one are plotted in Fig. 3: both spheres are located at the same height z above the no-slip wall, the vector of length r connecting the sphere centers pointing along the x-direction.

for $r \gg z$ for HI along the connection vector in Fig. 3(a); the strength of HI perpendicular to this axis decays faster ($\propto 1/r^5$), see Figs. 3(b) and 3(c). Note also the sign change in μ_{zz}^{RPB} in Fig. 3(c) which turns from positive to negative for $r \approx 0.9z$ for distances $z \gg a$.

To characterize the strength of HI for a certain relative configuration of two spheres, we define the following scalar quantity:

$$H(r,z) \equiv \sqrt{\frac{1}{3}\sum_{\alpha,\beta=1}^{3} \mu_{\alpha\beta}^{\mathrm{RPB}\,2}}, \quad \langle \boldsymbol{v}^2 \rangle = \langle \boldsymbol{f}^{\mathrm{T}} \cdot \overleftrightarrow{\boldsymbol{\mu}}^{\mathrm{RPB\,T}} \cdot \overleftrightarrow{\boldsymbol{\mu}}^{\mathrm{RPB}} \cdot \boldsymbol{f} \rangle \equiv H^2(r,z)\,|\boldsymbol{f}|^2, \quad (12)$$

which relates the average mean-squared velocity of one sphere, $\sqrt{\langle \boldsymbol{v}^2 \rangle}$, to the magnitude $|\boldsymbol{f}|$ of the force acting on the other one, and where $\langle \ldots \rangle$ denotes an average over all possible directions of the force. Dynamic scaling regimes in the motion of semiflexible polymers result from a subtle interplay of HI and monomer mobility, which both decrease when approaching the no-slip boundary: as is visible from the Langevin Eq. (14) underlying the Brownian dynamics (BD) simulation method (cf. Sec. III A) as well as from the theoretical dynamic description in Sec. III B, a simultaneous drop of HI *and* self-mobilities by the same factor is equivalent to a rescaling of time and thus does not affect dynamic scaling exponents; in turn, in order to see non-trivial dynamic effects embodied in changes of dynamic scaling exponents, the ratio between self- and cross-mobility must change. The unitless ratio,

$$h(r,z) \equiv \frac{H(r,z)}{\sqrt{\frac{1}{3}\left(2(\mu_{\parallel}^{\mathrm{RPB}}(z))^2 + (\mu_{\perp}^{\mathrm{RPB}}(z))^2\right)}} \cdot \frac{\mu_0}{\lim_{z\to\infty} H(r,z)}, \quad (13)$$

thus quantifies the relative importance of hydrodynamics at a finite distance z from a no-slip boundary compared to an unbounded fluid. For the configuration shown in Fig. 2, the function h in Eq. (13) is plotted for different values of the separation z in Fig. 3(d). In the limit of large separations from the wall, $z \to \infty$, full HI described by the Rotne-Prager tensor[20] $\overleftrightarrow{\boldsymbol{\mu}}^{\mathrm{RP}}$ [cf. Eq. (A2) in the Appendix] are recovered

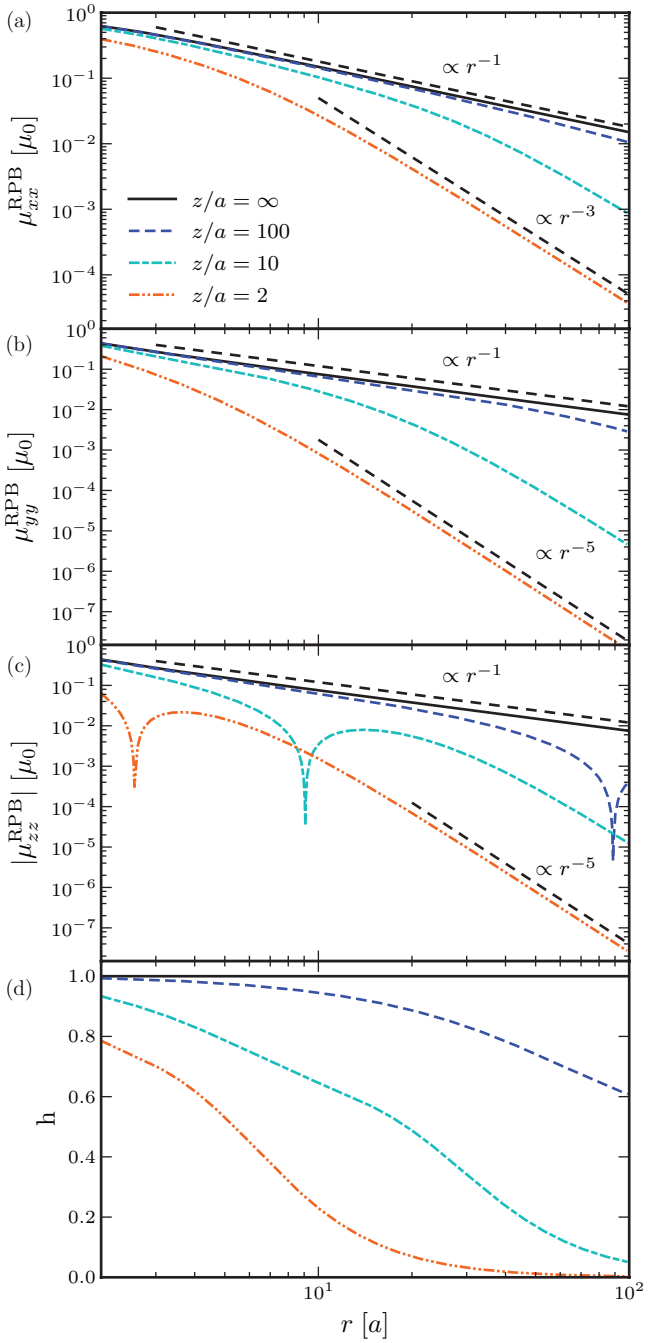

FIG. 3. Screened hydrodynamic interactions (HI) between spherical particles of radius a situated at a relative distance r from each other in the x-direction and at equal height z above a no-slip interface (see Fig. 2). Panels (a)–(c): The diagonal entries of the Rotne-Prager level of the Blake tensor specified in the Appendix [Eqs. (A1)–(A5)] are shown for different distances z from the wall (color lines); in the limit $z \to \infty$ the usual Rotne-Prager tensor (see Ref. 20), detailed in the Appendix in Eq. (A2), is recovered (solid black line). A crossover from a scaling $\propto 1/r$ to $\propto 1/r^3$ and $\propto 1/r^5$ for cross-mobilities parallel and perpendicular to the connection vector is induced by the no-slip boundary condition at the wall. Panel (d): For the same values of z as above the relative importance of HI compared to an unbounded fluid is quantified in terms of the unitless function h defined in Eq. (13).

($h = 1$), while the free-draining limit corresponds to $h = 0$. As is clearly seen in Fig. 3(d), the influence of HI is continuously reduced with increasing inter-bead separation r and decreasing distance to the wall z compared to the case of an unbounded fluid, though for small inter-bead separations it remains sizeable even for $z/a = 2$. The consequences arising from this complex behavior of HI and self-mobilities for the dynamics of semiflexible polymers in the vicinity of a no-slip boundary are presented and discussed in Sec. IV.

III. METHODS

A. Hydrodynamic simulations

The dynamics of a semiflexible polymer in solution is simulated adopting a standard hydrodynamic BD scheme,[25] in which the polymer is modeled as a chain of M beads of radius a. For the low Reynolds number regime, the Langevin equation governing the time evolution of the position $\boldsymbol{r}_i = (x_i, y_i, z_i)^{\mathrm{T}}$ of bead i is given by

$$\frac{d\boldsymbol{r}_i(t)}{dt} = \sum_{j=1}^{M} \overleftrightarrow{\boldsymbol{\mu}}_{ij} \cdot (-\nabla_{\boldsymbol{r}_j} U(\boldsymbol{r}_1, \ldots, \boldsymbol{r}_M)) + k_{\mathrm{B}}T \left[\frac{\mathrm{d}\mu_{\perp}^{\mathrm{RPB}}(z)}{\mathrm{d}z}\right]_{z=z_i} \hat{z} + \boldsymbol{\xi}_i(t), \qquad (14)$$

where $\hat{z}$ denotes the unit vector in the z-direction. The mobility matrix $\overleftrightarrow{\boldsymbol{\mu}}$ composed of the 3×3-submatrices

$$\overleftrightarrow{\boldsymbol{\mu}}_{ij} = \overleftrightarrow{\boldsymbol{\mu}}_{\mathrm{self}}^{\mathrm{RPB}}(z_i)\delta_{ij} + (1 - \delta_{ij})\overleftrightarrow{\boldsymbol{\mu}}^{\mathrm{RPB}}(\boldsymbol{r}_i, \boldsymbol{r}_j), \qquad (15)$$

accounts for two effects: (i) the dependence of the self-mobility on the distance z_i of bead i from the wall [cf. Eqs. (7)–(9)], and (ii) the fact that a force $\boldsymbol{f}_j \equiv -\nabla_{\boldsymbol{r}_j} U$ acting on bead j creates a hydrodynamic flow-field in the fluid thereby entraining bead i [cf. Eq. (6)]. The second term in Eq. (14) is due to the spatial variation of the beads' self-mobilities; it is introduced to compensate the flux caused by the position dependent random velocity contributions $\boldsymbol{\xi}_i$,[25,26] which are assumed to be Gaussian random vectors with hydrodynamic correlations according to the fluctuation-dissipation theorem,

$$\langle \boldsymbol{\xi}_i(t) \otimes \boldsymbol{\xi}_j(t') \rangle = 2k_{\mathrm{B}}T \overleftrightarrow{\boldsymbol{\mu}}_{ij} \delta(t - t'). \qquad (16)$$

The potential $U = U_{\mathrm{WLC}} + U_{\mathrm{LJ}} + U_{\mathrm{conf}}$ determining the configuration-dependent forces felt by the beads consists of three terms

$$U_{\mathrm{WLC}} = \frac{\gamma}{4a} \sum_{i=1}^{M-1} (r_{i+1,i} - 2a)^2 + \frac{\kappa}{2a} \sum_{i=2}^{M-1} (1 - \cos\theta_i),$$

$$U_{\mathrm{LJ}} = w \sum_{i<j} \Theta(2a - r_{ij}) \left[\left(\frac{2a}{r_{ij}}\right)^{12} - 2\left(\frac{2a}{r_{ij}}\right)^{6} + 1\right],$$

$$U_{\mathrm{conf}} = \frac{g}{2} \sum_{i=1}^{M} (z_i - z_0)^2, \qquad (17)$$

where $r_{ij} = |\boldsymbol{r}_i - \boldsymbol{r}_j|$ denotes the separation between the centers of beads i and j, and θ_i is the angle between the bond vectors connecting beads $i - 1$ and i, and beads i and $i + 1$, respectively. The shifted harmonic potential between adjacent beads of strength $\gamma = 200k_{\mathrm{B}}T/a$ keeps the contour length $L = (M - 1)2a$ approximately fixed, a bending potential of strength κ between adjacent bonds takes care of the bending stiffness of the chain, and the pairwise truncated repulsive

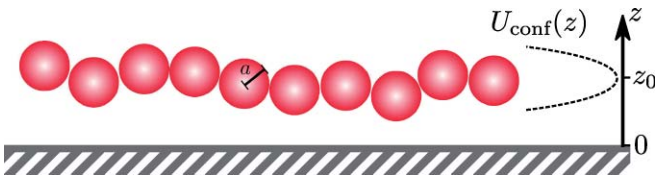

FIG. 4. Schematic illustration of the simulation setup: A polymer chain consisting of M monomers of radius a is confined by the harmonic potential $U_{\rm conf}$ [Eq. (17)] centered around z_0 acting in the z-direction; the strength of HI varies depending on the separation z from the wall.

Lennard-Jones potential $U_{\rm LJ}$ of strength $w = 3k_{\rm B}T$ prevents significant bead overlap, which otherwise would be a source of numerical instabilities. The harmonic potential $U_{\rm conf}$ of strength $g = 1k_{\rm B}T/a^2$ centered around z_0 keeps the average distance of the polymer beads from the wall fixed; the simulation setup is schematically illustrated in Fig. 4. By gradually varying the value of z_0, the influence of the hydrodynamic boundary condition at the wall on the motion of the polymer is sensitively resolved. In the limit of infinite separation from the wall, the usual Rotne-Prager tensor,[20] specified in Eq. (A2) in the Appendix, is recovered as hydrodynamic interaction tensor.

Eq. (14) is discretized and integrated numerically using a simple Euler algorithm; the time discretized form of the Langevin equation for bead i reads

$$\boldsymbol{r}_i(t+\Delta t) = \boldsymbol{r}_i(t) + \left(\sum_{j=1}^{M} \overleftrightarrow{\boldsymbol{\mu}}_{ij} \cdot \boldsymbol{f}_j + k_{\rm B}T \left[\frac{{\rm d}\mu_{\perp}^{\rm RPB}(z)}{{\rm d}z} \right]_{z=z_i} \hat{z} \right) \Delta t + \Delta \boldsymbol{r}_i^{\rm ran}(t), \quad (18)$$

where the time step is denoted by Δt, and the stochastic contributions $\Delta \boldsymbol{r}_i^{\rm ran}$ are Gaussian distributed random vectors with vanishing mean and correlations $\langle \Delta \boldsymbol{r}_i^{\rm ran}(t) \otimes \Delta \boldsymbol{r}_j^{\rm ran}(t) \rangle = 2\,k_{\rm B}T\, \overleftrightarrow{\boldsymbol{\mu}}_{ij} \Delta t$. In the case of collisions with the wall, the z-component is reflected about $z = a$, while the updating scheme for the other components remains unchanged. The correlated stochastic contributions of Eq. (16) are obtained from uncorrelated Gaussian noise by means of a Cholesky decomposition of the hydrodynamic matrix $\overleftrightarrow{\boldsymbol{\mu}}$. In all the results below, lengths are measured in units of the bead radius a, energies in units of thermal energy $k_{\rm B}T$ and time in units of $\tau \equiv a^2/(k_{\rm B}T\mu_0)$.

B. Hydrodynamic mean field theory

For the theoretical description of the polymer motion, we apply a dynamic mean field approach which has proven useful for the description of semiflexible polymer dynamics in three dimensions in various contexts ranging from DNA end-monomer diffusion[4,5] to DNA-protein binding dynamics.[27]

The simplest description of a semiflexible polymer is the wormlike chain (WLC) model: the polymer is represented by a continuous, differentiable space curve $\boldsymbol{r}(s)$ of contour length L. The associated elastic energy $U_{\rm WLC}$, the continuum analogue of Eq. (17), is given by[28]

$$U_{\rm WLC}[\boldsymbol{r}(s)] = \frac{\kappa}{2} \int_{-L/2}^{L/2} {\rm d}s \, \left(\frac{\partial \boldsymbol{u}(s)}{\partial s} \right)^2. \quad (19)$$

Here, the arc-length variable ranging from $-L/2$ to $L/2$ is denoted by s, and the tangent vector $\boldsymbol{u} \equiv \partial \boldsymbol{r}/\partial s$ is constrained by local inextensibility to unit length, $\boldsymbol{u}^2(s) = 1\ \forall\, s$. The bending rigidity κ is related to the persistence length $l_{\rm p}^{d{\rm D}}$, the typical length scale on which tangent-tangent correlations decay

$$\langle \boldsymbol{u}(s) \cdot \boldsymbol{u}(s') \rangle = \exp\left(-\frac{|s-s'|}{l_{\rm p}^{d{\rm D}}} \right), \quad l_{\rm p}^{d{\rm D}} \equiv \frac{2\kappa}{(d-1)k_{\rm B}T}, \quad (20)$$

where d is the dimension. In this paper we consider the case of two-dimensional confinement ($d = 2$); the configurational space being reduced compared to three dimensions, a polymer with given bending rigidity κ therefore appears stiffer in confinement: $l_{\rm p} \equiv l_{\rm p}^{3{\rm D}} = l_{\rm p}^{2{\rm D}}/2$.

The constraint in the tangent vector length leading to nonlinear equations of motion, an alternative, approximate model is required. Within a mean field approach[29,30] the local constraint is relaxed and replaced by the global and end-point conditions $\langle \int {\rm d}s\, \boldsymbol{u}^2(s) \rangle = L$ and $\langle \boldsymbol{u}^2(\pm L/2) \rangle = 1$. The resulting Gaussian mean field Hamiltonian incorporates a finite extensibility in addition to the bending term,

$$U_{\rm MF}[\boldsymbol{r}(s)] = \frac{\epsilon}{2} \int_{-L/2}^{L/2} {\rm d}s \, \left(\frac{\partial \boldsymbol{u}(s)}{\partial s} \right)^2 + \nu \int_{-L/2}^{L/2} {\rm d}s \, \boldsymbol{u}^2(s) + \nu_0 (\boldsymbol{u}^2(L/2) + \boldsymbol{u}^2(-L/2)), \quad (21)$$

where the MFT parameters

$$\epsilon = l_{\rm p}^{2{\rm D}} k_{\rm B}T, \quad \nu = \frac{k_{\rm B}T}{2 l_{\rm p}^{2{\rm D}}}, \quad \text{and} \quad \nu_0 = \frac{k_{\rm B}T}{2}, \quad (22)$$

are chosen such that the most important static equilibrium quantities of the WLC, the tangent-tangent correlation function in Eq. (20) and other derived quantities, such as the mean squared end-to-end distance, are correctly reproduced.[31]

The dynamic theory for the Gaussian semiflexible polymer is based on the hydrodynamic preaveraging approach,[32] analogous to that used for the Zimm model[33] in the case of flexible chains. Within that approximation, the time evolution of the position-vector of point s on the polymer contour within the x-y-plane is governed by the Langevin equation,

$$\frac{\partial}{\partial s} \boldsymbol{r}(s,t) = -\int_{-L/2}^{L/2} {\rm d}s' \, \overleftrightarrow{\boldsymbol{\mu}}_{\rm avg}(s,s';z) \frac{\delta U_{\rm MF}}{\delta \boldsymbol{r}(s',t)} + \boldsymbol{\xi}(s,t),$$
$$\langle \boldsymbol{\xi}(s,t) \otimes \boldsymbol{\xi}(s',t') \rangle = 2k_{\rm B}T\, \overleftrightarrow{\boldsymbol{\mu}}_{\rm avg}(s,s';z)\, \delta(t-t'). \quad (23)$$

Here the preaveraged mobility tensor $\overleftrightarrow{\boldsymbol{\mu}}_{\rm avg}$ is used, which is a function of the contour points s and s' only and does not depend on the actual spatial positions $\boldsymbol{r}(s,t)$ and $\boldsymbol{r}(s',t)$. The preaveraged tensor is given by

$$\overleftrightarrow{\boldsymbol{\mu}}_{\rm avg}(s,s';z) = \left[2a\mu_{\parallel}^{\rm RPB}(z)\delta(s-s') + \Theta(|s-s'|-2a) \times \mu_{\rm avg}^{\rm RPB}(s,s';z) \right] \overleftrightarrow{\boldsymbol{1}}, \quad (24)$$

thus incorporating the self-mobility $\mu_{\parallel}^{\mathrm{RPB}}$ parallel to the boundary [Eq. (8)], and the preaveraged HI between different parts of the polymer contour $\mu_{\mathrm{avg}}^{\mathrm{RPB}}$, which are cut off for distances $|s-s'|<2a$ by the unit step function Θ; in Eq. (24), the 2×2 identity matrix is denoted by $\overleftrightarrow{\mathbf{1}}$. The preaveraged HI are obtained by averaging the 2×2 sub-block of the Rotne-Prager level of the Blake tensor [Eq. (6)] corresponding to the x- and y-components over all equilibrium configurations of the polymer,

$$\overleftrightarrow{\boldsymbol{\mu}}_{\mathrm{avg}}^{\mathrm{RPB}}(s,s';z)=\int \mathrm{d}^2 r\ \overleftrightarrow{\boldsymbol{\mu}}^{\mathrm{RPB}}(\boldsymbol{r};z)P_{\mathrm{eq}}(\boldsymbol{r};s,s') = \mu_{\mathrm{avg}}^{\mathrm{RPB}}(s,s';z)\overleftrightarrow{\mathbf{1}}, \tag{25}$$

where a Gaussian equilibrium distribution of (two-dimensional) distances $\boldsymbol{r}$ between s and s' is used,

$$P_{\mathrm{eq}}(\boldsymbol{r};s,s')=\frac{1}{\pi\sigma(s-s')}\exp\left(-\frac{\boldsymbol{r}^2}{\sigma(s-s')}\right),$$
$$\sigma(\Delta s)\equiv 2l_{\mathrm{p}}^{2\mathrm{D}}(\Delta s - l_{\mathrm{p}}^{2\mathrm{D}}(1-\mathrm{e}^{-\Delta s/l_{\mathrm{p}}^{2\mathrm{D}}})). \tag{26}$$

Note that the steric effect of the wall need not be accounted for, since the polymer distribution is restricted to a two-dimensional layer. The explicit functional form of $\mu_{\mathrm{avg}}^{\mathrm{RPB}}$ appearing in Eqs. (24) and (25) is given in Eq. (A9) in the Appendix.

The preaveraged Langevin Eq. (23) can be solved through a normal mode decomposition, with the eigenmodes fulfilling free-end boundary conditions at $s=\pm L/2$. Since the MFT parameters (Eq. (22)) are all just multiplied by the constant factor 2/3 compared to three dimensions, the free-end boundary conditions and the form of the normal modes described in detail elsewhere[4] remain unchanged. The eigenmode expansion yields a set of ordinary differential equations coupled by a hydrodynamic interaction matrix; once this matrix is diagonalized,[4,33] the problem is reduced to simple Langevin equations for the decoupled normal mode amplitudes $\boldsymbol{P}_n(t)$ with stochastic contributions $\boldsymbol{Q}_n(t)$,

$$\frac{\partial}{\partial t}\boldsymbol{P}_0(t)=\boldsymbol{Q}_0(t),$$
$$\frac{\partial}{\partial t}\boldsymbol{P}_n(t)=-\Lambda_n\boldsymbol{P}_n(t)+\boldsymbol{Q}_n(t),\quad n=1,\ldots,N, \tag{27}$$
$$\langle Q_n(t)\otimes Q_m(t')\rangle = 2k_{\mathrm{B}}T\delta_{nm}\delta(t-t')\Theta_n\overleftrightarrow{\mathbf{1}}.$$

The vectors $\boldsymbol{P}_n(t)$ and $\boldsymbol{Q}_n(t)$ are related to the polymer conformation $\boldsymbol{r}(s,t)$ and to the stochastic velocities $\boldsymbol{\xi}(s,t)$ through the expansions

$$\boldsymbol{r}(s,t)=\sum_{n=0}^{N}\boldsymbol{P}_n(t)\Psi_n(s),\quad \boldsymbol{\xi}(s,t)=\sum_{n=0}^{N}\boldsymbol{Q}_n(t)\Psi_n(s), \tag{28}$$

where the scalar functions $\Psi_n(s)$ are the decoupled normal modes. The modes are ordered in such a way that the eigenvalues Λ_n (inverse relaxation times) increase with n. We set the high-frequency cutoff N for the mode number to $N=\lceil L/8a\rceil$, which was previously shown to give good agreement at small scales with BD simulations in three dimensions.[4,27] The precise choice of the mode number cutoff does not influence the polymer motion on length scales much larger than the monomer radius a and is therefore only relevant on time scales $t\lesssim\tau$. The inverse relaxation times Λ_n and the fluctuation-dissipation parameters Θ_n can directly be derived from the tensor $\overleftrightarrow{\boldsymbol{\mu}}_{\mathrm{avg}}^{\mathrm{RPB}}$ evaluated numerically in the normal mode basis. Full details of this procedure together with the explicit form of the normal modes $\Psi_n(s)$ were given before.[4]

Using the Langevin equations in Eq. (27) and the normal mode decomposition in Eq. (28), the MSD of the polymer's ends Δ_{e}^2 and the MSD of the end-to-end vector Δ_{ee}^2 are readily calculated, yielding

$$\Delta_{\mathrm{e}}^2(t)\equiv\langle(\boldsymbol{r}(\pm L/2,t)-\boldsymbol{r}(\pm L/2,0))^2\rangle = 4D_{\mathrm{pol}}^{2\mathrm{D}}t+4k_{\mathrm{B}}T\sum_{n=1}^{N}\frac{\Theta_n}{\Lambda_n}\Psi_n^2(\pm L/2)(1-\mathrm{e}^{-\Lambda_n t}), \tag{29}$$

$$\Delta_{\mathrm{ee}}^2(t)\equiv\langle((\boldsymbol{r}(L/2,t)-\boldsymbol{r}(-L/2,t)) -(\boldsymbol{r}(L/2,0)-\boldsymbol{r}(-L/2,0)))^2\rangle = 4k_{\mathrm{B}}T\sum_{n=1,\,\mathrm{odd}}^{N}\frac{\Theta_n}{\Lambda_n}(\Psi_n(L/2) -\Psi_n(-L/2))^2(1-\mathrm{e}^{-\Lambda_n t}), \tag{30}$$

where the center-of-mass diffusion constant of the polymer is

$$D_{\mathrm{pol}}^{2\mathrm{D}}\equiv k_{\mathrm{B}}T\Theta_0\Psi_0^2(\pm L/2). \tag{31}$$

The temporal dependence of the dynamic quantities in Eqs. (29) and (30) for different distances z from the no-slip wall are compared to BD results in Sec. IV.

IV. RESULTS AND DISCUSSION

Extensive hydrodynamic BD simulations of polymers of contour length $L=100\,a$ (corresponding to $M=51$ beads) and (three-dimensional) persistence lengths l_{p} ranging from 40 to $320\,a$ were performed at various average distances z_0 from the wall; a simulation snapshot showing polymer conformations at different distances from the wall is found in Fig. 5.

The simulation time step was set to $\Delta t=0.06\,a/(\mu_0\gamma)$, corresponding to $\Delta t=3\times 10^{-4}\,\tau$ for the stretching parameter $\gamma=200k_{\mathrm{B}}T/a$, which was used in all hydrodynamic and most of the free-draining simulations. Each trajectory lasted $3\times 10^5\,\tau$, after an initial thermalization period of $3\times 10^3\,\tau$. For each parameter set, the observables of interest were averaged along each trajectory and over up to 16 independent simulation runs. For comparison, we also performed free-draining BD simulations, using a diagonal hydrodynamic matrix $\overleftrightarrow{\boldsymbol{\mu}}_{ij}=\mu_0\delta_{ij}\overleftrightarrow{\mathbf{1}}$ in Eqs. (15) and (16), and also set up a free-draining version of the MFT by replacing Eq. (24) by $\overleftrightarrow{\boldsymbol{\mu}}_{\mathrm{avg}}(s,s')=2a\mu_0\delta(s-s')\overleftrightarrow{\mathbf{1}}$, where μ_0 is the bare mobility of a sphere of radius a (at infinite distance from the confining plane).

We first discuss the time dependence of the end-monomer and the end-to-end vector MSDs [Eqs. (29) and (30)] and their sensitivity to bending stiffness and hydrodynamic screening: as is illustrated in the graph in Fig. 5, the end-monomer

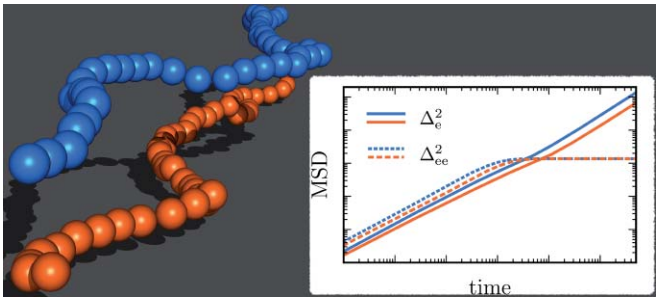

FIG. 5. BD simulation snapshot showing conformations of a polymer consisting of 51 beads (contour length $L = 100\,a$) and persistence length $l_p = 40\,a$ subject to a harmonic confining potential centered around $z_0 = 10\,a$ (blue) and $z_0 = 2a$ (orange). The graph displays MFT results for the end-monomer MSD Δ_e^2 (Eq. (29), solid lines), which for long times reduces to the center of mass MSD $4D_{pol}^{2D}t$ [cf. Eq. (31)], and the end-to-end vector MSD (Eq. (30), broken lines), which in the long time limit levels off at twice the mean squared end-to-end distance $\sigma(L)$ [cf. Eq. (26)].

MSD Δ_e^2 reduces to the center-of-mass MSD, $4D_{pol}^{2D}t$, once the largest relaxation time Λ_1^{-1} is reached, while the end-to-end vector MSD Δ_{ee}^2 levels off at twice the equilibrium mean squared end-to-end distance $\sigma(L)$ [cf. Eq. (26)] for times $t \gtrsim \Lambda_1^{-1}$.

The end-monomer MSD Δ_e^2 in the x-y-plane for polymers of contour length $L = 100\,a$ and four different persistence lengths l_p are shown in the upper panels of Fig. 6: symbols denote hydrodynamic and free-draining simulation results, the lines correspond to the MFT expression given in Eq. (29). The overall agreement between simulations and MFT is good, in agreement with our previous results for the bulk case.[4–6] Note that no fitting parameter is used in the MFT. Two distinct effects are clearly identified in both simulation and theory: (i) when decreasing the distance to the wall, the curves are shifted to larger times, i.e., the overall dynamics are slowed down and (ii) the slope of the curves on the double-logarithmic scale corresponding to the exponent of the underlying power law decreases. These are non-trivial effects, since they depend on the subtle interplay between wall-induced self-mobility and HI, which both decrease when approaching the wall as shown in Figs. 1 and 3. Since the curves in the double-logarithmic representation show deviations from perfect straight lines, we adopt the concept of a local exponent,[4] which for a general function $f(t)$ is defined as

$$\alpha(t) \equiv \frac{d \log f(t)}{d \log t}. \tag{32}$$

The time dependent local exponent $\alpha(t)$ is estimated at each time t by fitting straight lines to the double logarithmic plot of MSD data points at times t_i within a small range around t, defined by the condition $|\log_{10}(t_i/t)| < 0.15$; the local exponents of the end-point MSDs are shown in the lower panels of Fig. 6. For short times, they exhibit extended plateaus over several decades, while a crossover to the center-of-mass exponent 1 takes place at times beyond the largest relaxation time Λ_1^{-1} of the polymer. The largest relaxation times, which are designated by vertical arrows in Figs. 6 and 7, increase by approximately a factor 5 when HIs are turned off. Note that even for times shorter than Λ_1^{-1} the exponents start to oscillate, these extended crossover regions reflect rotations of the entire polymer which for stiff filaments is captured by the first eigenmode.[5,31] Insufficient sampling leads to statistical noise in the simulated local exponents for times $t \gtrsim 10^3\,\tau$, such that the crossovers are only partially seen in the simulation data. When decreasing the distance to the wall, the values of the exponent are continuously reduced, approaching the scaling behavior of the free-draining limit, where for very stiff polymers without HI a typical scaling exponent of 3/4 is expected.[4,32] We briefly recall our previous results for the scale-dependent dynamics of semiflexible polymers in bulk.[4–6] In the weak stiffness range $a < l_p < L$, the exponent α for the end-point MSD was shown to change continuously as a function of time and to show a pronounced minimum roughly at the largest internal polymer time scale. Only in the limit $a \ll L \ll l_p$ asymptotic scaling is observed and in the absence of HI, the classical wormlike-chain exponent $\alpha \approx 3/4$ is realized for times $t < \Lambda_1^{-1}$. In the presence of HI, all exponents are increased by a constant shift of roughly 0.1 and thus the asymptotic wormlike-chain exponent is more of the order $\alpha \approx 0.85$. Those results from hydrodynamic simulations and hydrodynamic MFT could be rationalized by scaling theory and eigenmode analysis[4] and quantitatively compared with experimental time-resolved data for DNA.[5,6]

Remarkably, the dynamic crossover from hydrodynamic to free-draining behavior in Fig. 6 sets in at relatively small distances z_0 from the wall; in fact, the dynamics for $z_0 = 2a$, i.e., at a monomeric separation of the polymer from the wall, are characterized by a considerably higher slope than the free-draining one, meaning that HI—though screened—still contribute substantially to the relaxation dynamics. Note that this is *not* an artifact due to the use of approximate self-mobilities and HI of finite sized beads in hydrodynamic simulations and the MFT, since even at separations of two monomer radii from the wall these approximations compare well to the exact expressions (cf. Fig. 1). Similar trends are seen in the MSD of the end-to-end vector Δ_{ee}^2 in Fig. 7, which saturates at twice the average squared end-to-end distance of the polymer for $t \gg \Lambda_1^{-1}$; again a slowdown of the dynamics and a decrease of the local exponent are observed when HI are reduced due to the nearby wall; local slopes are reversely ordered due to this slowdown for $t \gtrsim \Lambda_1^{-1}$.

The quantitative agreement of the MSDs in BD simulations and in the MFT [Eqs. (29) and (30)] is less impressive in the confined geometry than in the three-dimensional case,[5] the MSDs generally being overestimated by the theory. The reasons for the reduced accuracy of the theory in the present case are manifold: (i) Within the MFT the polymer is treated as completely confined to two dimensions, while small out of plane fluctuations are possible in the simulations, (ii) as was argued in Ref. 5, long ranged HI are one factor for the success of the MFT in three dimensions; conversely, a worsening of the theory is thus expected in the present case, when the wall is approached and in consequence HI are gradually weakened (cf. Fig. 3), and (iii) in analogy with the critical behavior of lattice spin systems,[34] mean field theory and similarly also the preaveraging approximation of the hydrodynamic tensor are expected to perform better in higher dimension; the reduced accuracy of the two-dimensional theory can therefore

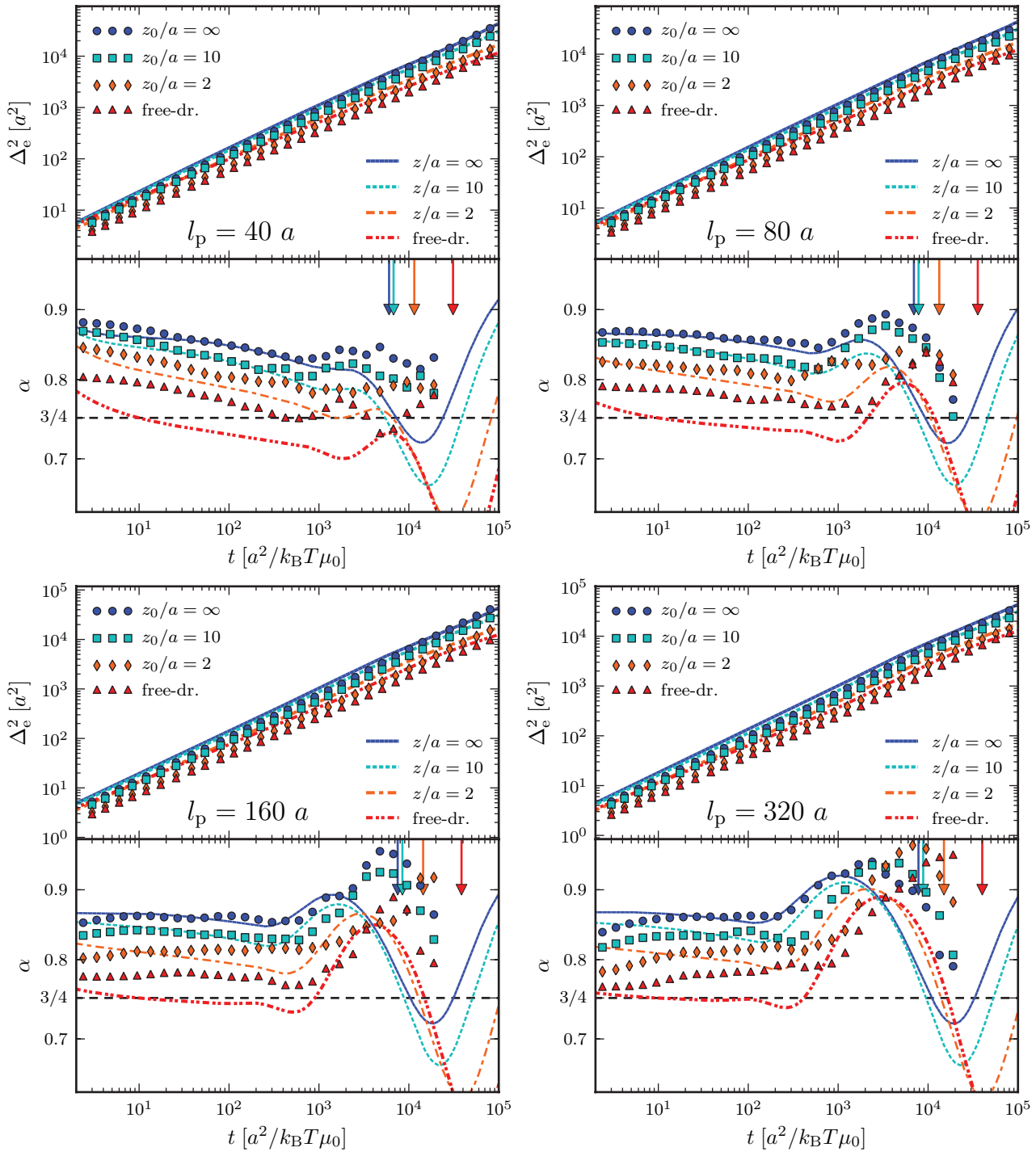

FIG. 6. In-plane dynamics of a polymer of length $L = 100\,a$ and (three-dimensional) persistence length l_p ranging from 40 to 320 a held at an average distance z_0 from a no-slip wall: end-monomer MSD (upper panels) and the corresponding local exponent α (*lower panels*) are shown. The *symbols* denote results from hydrodynamic and free-draining BD simulations, while the *lines* are results of the two dimensional MFT [Eq. (29)] for polymers at a distance z from the wall. Vertical arrows designate the largest MFT-relaxation times Λ_1^{-1}.

be, at least in part, attributed to the lower dimension. However, the general trends induced by the interaction with the no-slip boundary, which are seen best in the local exponents (lower panels of Figs. 6 and 7), are reliably reproduced by the MFT.

Considerably stiffer and longer chains, where the different dynamic regimes are clearly separated in time, are not accessible yet by means of simulations because of the overwhelming computational costs. In contrast, the mean field approach is equally applicable here. MFT results for a chain of length $L = 500\,a$ and $l_p = 500\,a$ shown in Fig. 8 confirm the previous observations: when approaching the wall, hydrodynamic screening shifts the crossovers to larger times and simultaneously decreases the (local) exponent, though not quite reaching the free-draining limit with exponent 3/4 even at wall separations on the order of the monomer size.

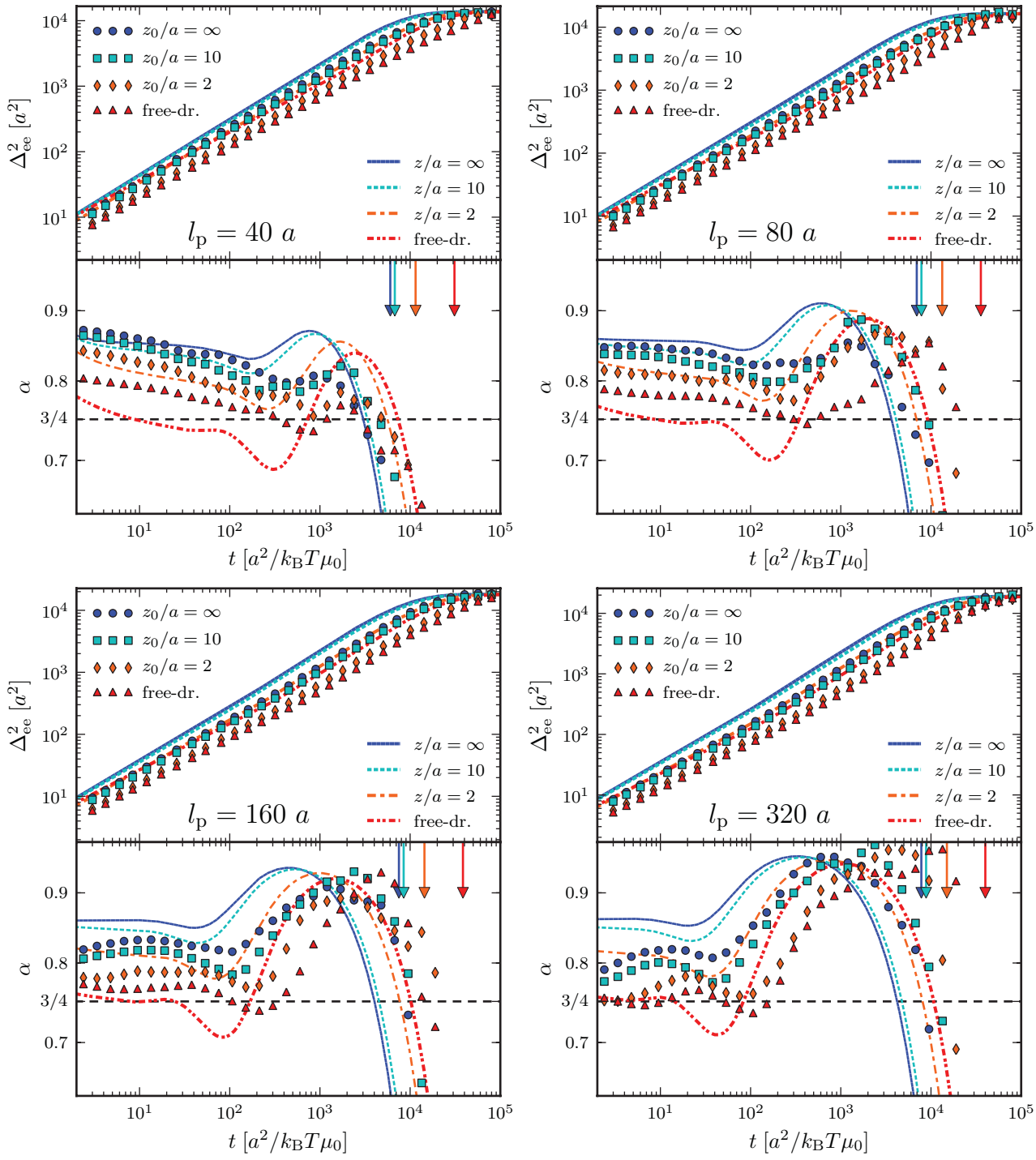

FIG. 7. Same as Fig. 6, but showing the end-to-end vector MSD [Eq. (30)] (upper panels) and the corresponding local exponent α (lower panels).

Clearly, the strength of HI is the most relevant parameter for determining the dynamic scaling exponents in Figs. 6–8, while the ratio l_p/L, ranging from 0.4 to 3.2, is of comparatively minor importance for the MSDs of the vectorial quantities considered so far.

Experimentally, end-to-end relaxation dynamics were studied using end-labeled f-actin filaments,[10] which were enclosed in a 1μm thick chamber to keep the fluorescent markers in the focal plane of the microscope. The dynamics of filaments of contour lengths L ranging from 5.9 to 25.6μm and persistence length $l_p \approx 15.7\mu$m (Ref. 10) was quantified in terms of the MSD of the (scalar) end-to-end distance,

$$\Delta^2_{see} \equiv \langle (R(t) - R(0))^2 \rangle, \quad R(t) \equiv |\boldsymbol{r}(L/2, t) - \boldsymbol{r}(-L/2, t)|, \tag{33}$$

which obviously differs from the end-to-end vector MSD in Eq. (30); in their work Le Goff *et al.* suggested a linear rescaling of the time and MSD variables in order to collapse the

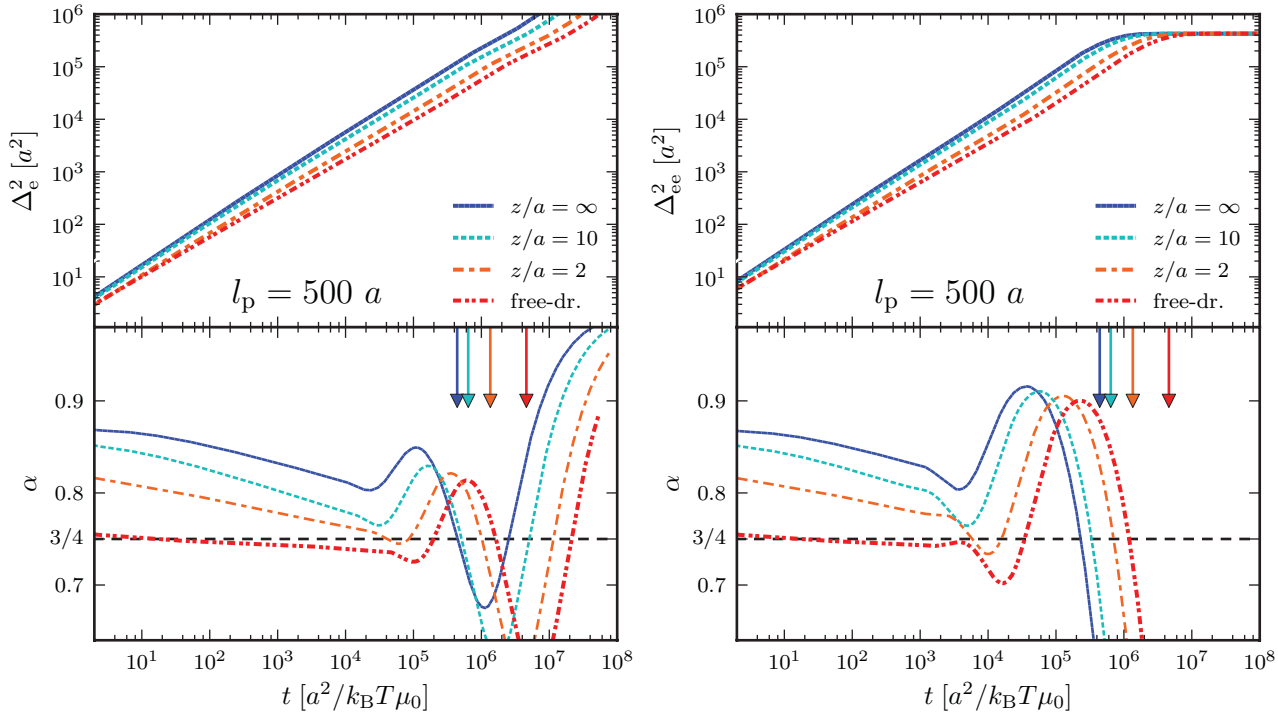

FIG. 8. MFT results for in-plane dynamics of a polymer of length $L = 500\,a$ and persistence length $l_p = 500\,a$: the upper panels show the end-monomer MSD [*left*, Eq. (29)] and the end-to-end vector MSD [*right*, Eq. (30)]; the lower panels show the corresponding local exponents α for various distances z from the wall as well as in the free-draining limit. Vertical arrows designate the largest MFT-relaxation times Λ_1^{-1}.

MSD dataset onto a single master curve, which at short times reduces to a power law scaling with exponent $\alpha = 3/4$. Interestingly, our reanalysis of the experimental data in terms of local slopes reveals smooth crossovers from values between 0.8 and 1.0 at short times to values around 0.7 before the slopes quickly drop towards 0. The original data as well as the corresponding local slopes, both affected by significant statistical noise, are shown in Fig. 9: plateau regions with an approximately constant exponent (cf. Figs. 6–8) are not observed. Note that when linearly rescaling time $\tilde{t} \equiv \beta t$ and the dynamic observable of interest $\tilde{f}(\tilde{t}) \equiv \zeta f(\beta t)$, the local exponent defined in Eq. (32) is unchanged, $\tilde{\alpha}(\tilde{t}) = \alpha(\beta t)$, so the rescaling cannot be the reason for the apparent exponent plateau seen in the original data analysis. Rather, the graphical averaging over the various filament lengths seems to wash out the variations of the exponent as a function of time and when comparing different filament lengths with each other.

Unfortunately, the isotropic mean field theory in the formulation in Sec. III B does not allow the evaluation of the scalar end-to-end distance MSD measured in the experiments. Also, a direct comparison of experiments and hydrodynamic simulations is unfeasible because of the immense computational costs associated with contour lengths $L/a \sim \mathcal{O}(10^3)$. The MSD of the scalar end-to-end distance from BD simulations of chain length $L = 100\,a$ are shown in Fig. 10. As in the case of the end-to-end vector MSD in Fig. 7, the weakening of HI leads to a slowdown of the overall relaxation dynamics, the saturation crossover being shifted to larger times; the scalar end-to-end distance, however, saturates at considerably smaller times since the slow rotational mode of the entire

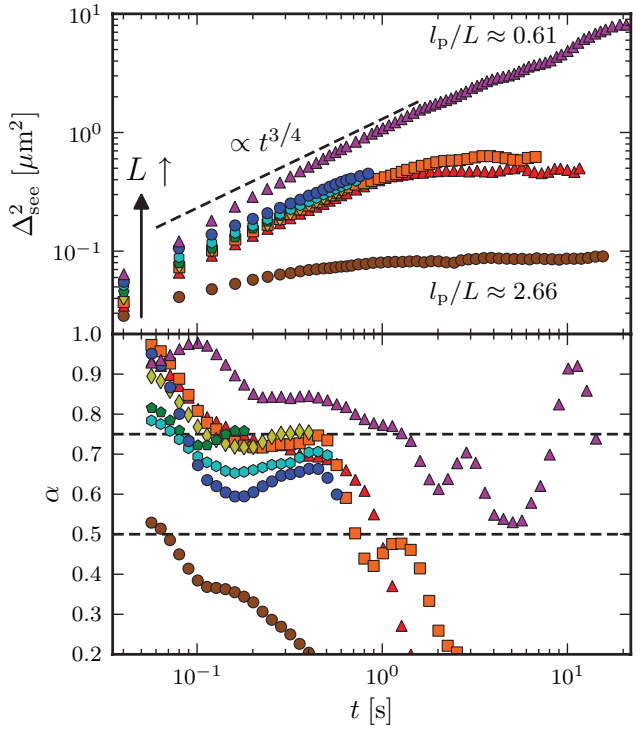

FIG. 9. (Upper panel) Experimental MSD of the scalar end-to-end distance of f-actin filaments of contour length $L =$ 5.9, 10.4, 10.7, 11.8, 11.8, 11.9, 12.9, and 25.6 μm (from bottom to top, data digitized from the inset of Fig. 3 in Ref. 10; since all data points were plotted using the same dot size in the original publication, only those parts of the dataset were used, which could unambigously be assigned to a certain contour length L). Assuming a (three-dimensional) persistence length $l_p \approx 15.7\,\mu$m, (see Ref. 10) the ratio l_p/L thus varies between 0.61 and 2.66 (from top to bottom). (Lower panel) Corresponding local slope α.

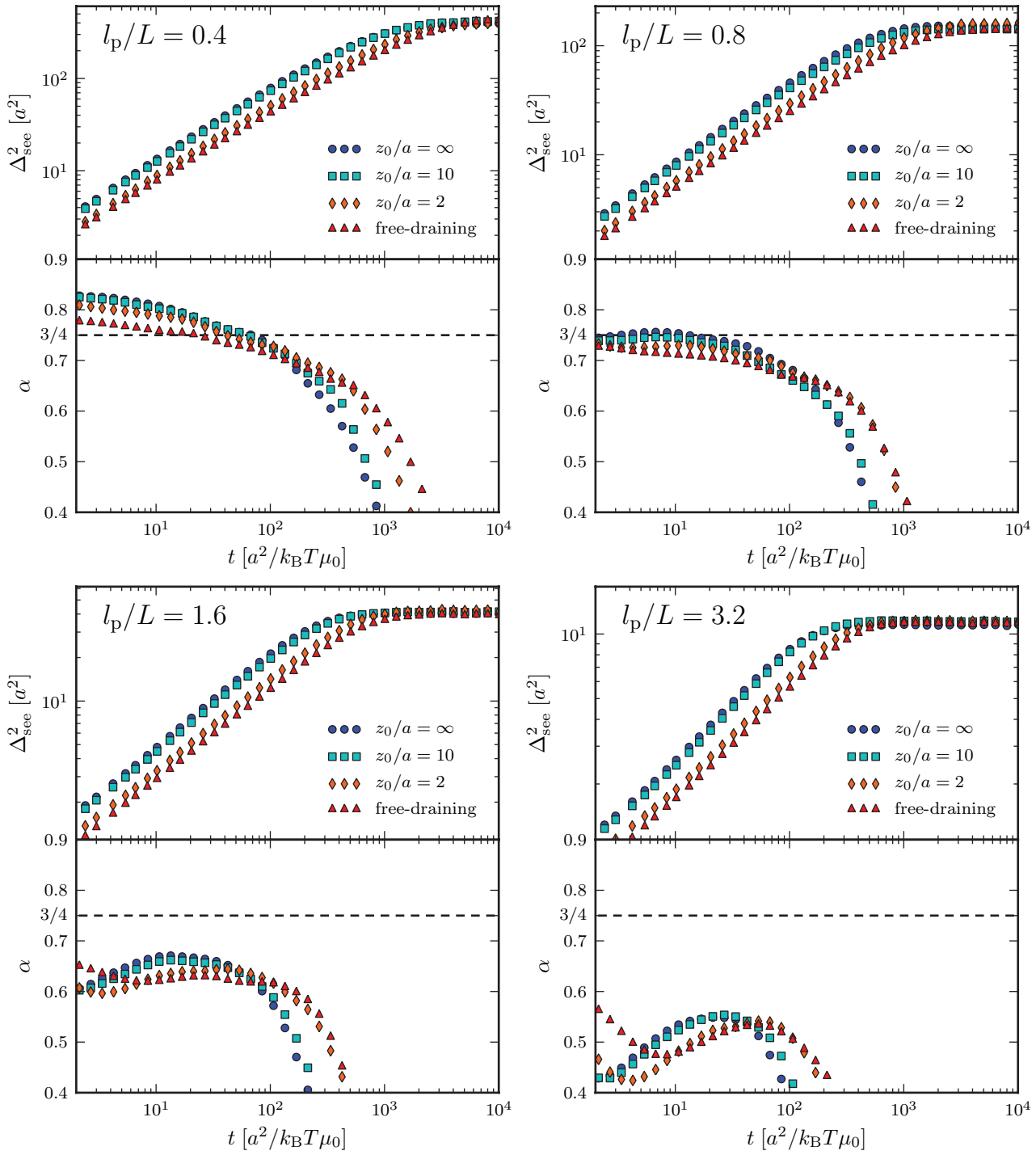

FIG. 10. Scalar end-to-end distance MSD extracted from hydrodynamic BD simulations of a polymer of length $L = 100\,a$ and varying stiffness l_p/L for several average distances z_0 from the confining wall (upper panels) as well as corresponding the local exponents α (lower panels). For comparison results from free-draining BD simulations are shown using *red triangles*.

filament is factored out in this observable. In accordance with the experimental data in Fig. 9, the local exponents are rather characterized by smooth crossovers than by constant values; most strikingly, the comparison of the simulation results in Fig. 10 reveals a strong dependence of the local exponents on the ratio l_p/L. Typical values of $\alpha \gtrsim 0.8$ for $l_p/L = 0.4$, $\alpha \approx 0.7 - 0.75$ for $l_p/L = 0.8$, $\alpha \approx 0.65$ for $l_p/L = 1.6$, and $\alpha \approx 0.5$ for $l_p/L = 3.2$ are identified, in agreement with results previously obtained for the fluctuations of unconstrained filaments.[5] For a fixed ratio l_p/L, the strength of HI varying with the distance z_0 from the boundary only slightly affects the local exponents, hydrodynamics thus seems to be of minor importance for the dynamic scaling of the scalar end-to-end distance MSD, in contrast to the vectorial MSDs in Figs. 6 and 7. This is not surprising, as hydrodynamics most strongly affect center-of-mass translation and rotation, both of which are factored out in the scalar end-to-end distance. This finding suggests to use free-draining simulations for a more detailed

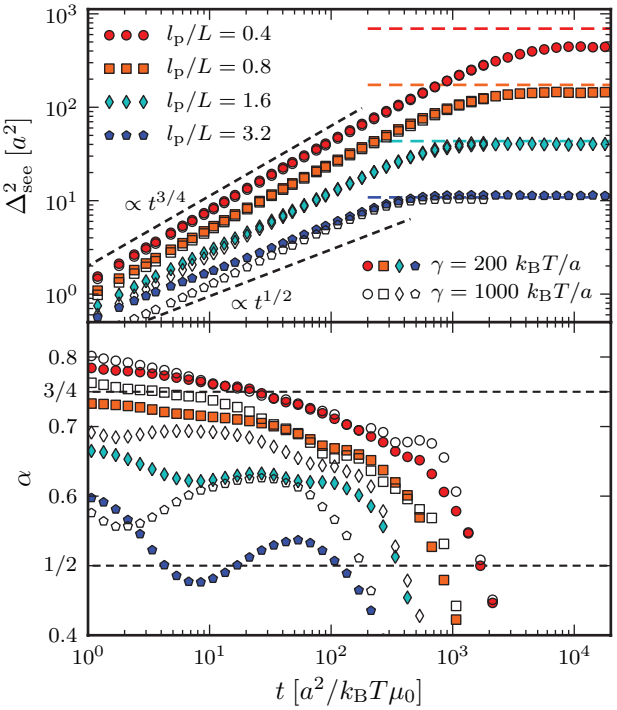

FIG. 11. Influence of stiffness l_p/L and stretching force constant γ on the end-to-end distance MSD [Eq. (33), upper panel] and corresponding local exponents (lower panel) in free-draining BD simulations of a polymer of length $L = 100\,a$. Results obtained with the standard stretching force constant $\gamma = 200\,k_BT/a$ (*filled symbols*) are compared to the same observables when employing $\gamma = 1000\,k_BT/a$ (*open symbols*).

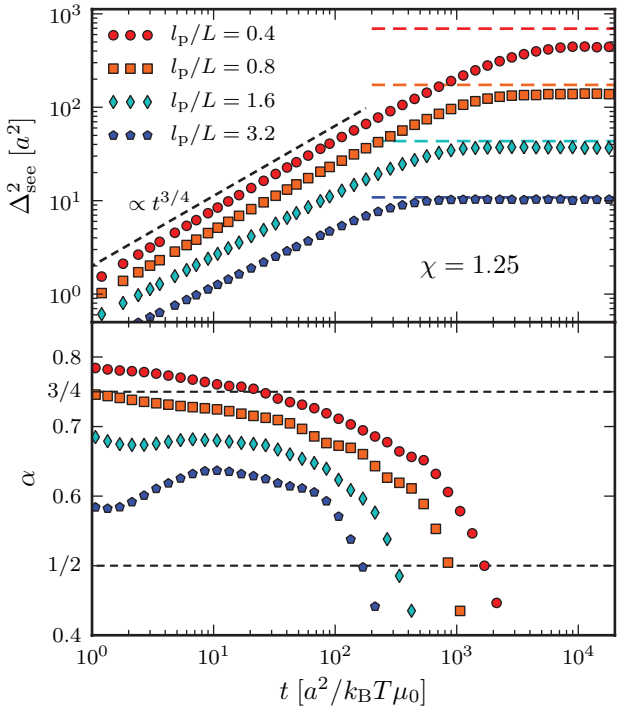

FIG. 12. (Upper panel) Influence of simultaneous variation of bending and stretching stiffness on the scalar end-to-end distance MSD [Eq. (33)] in free-draining BD simulations of a polymer of length $L = 100\,a$. Results are shown for polymers of different stiffness l_p/L, but constant χ defined in Eq. (34), corresponding to isotropic elastic cylinders. (*Lower panel*) Corresponding local exponents.

analysis of the dynamic scaling behavior of the scalar end-to-end distance.

The fact that the local slopes in Fig. 10 tend towards 1/2 instead of 3/4 with increasing ratio l_p/L is easily understood by realizing that we keep the harmonic bond-stretching parameter [cf. Eq. (17)] constant at a value $\gamma = 200\,k_BT/a$ in our simulations, while varying the bending stiffness κ; as a consequence, the free-draining scalar end-to-end relaxation becomes dominated by stretching relaxation[35] with characteristic exponent 1/2 in the limit $\kappa \to \infty$, where we note that the weakly bending wormlike chain exponent 3/4 is expected only in the idealized limit of a perfectly inextensible semiflexible chain. To substantiate this suggestion, we compare the scalar end-to-end MSDs of free-draining simulations with $\gamma = 200 k_BT/a$ and $\gamma = 1000\,k_BT/a$ in Fig. 11. Indeed, one finds higher slopes in the less extensible case, when employing a higher value of γ. In turn, variations of the chain extensibility only marginally affect end-to-end relaxation dynamics in the flexible regime $l_p/L \lesssim 1$, since here the relaxation is dominated by bending fluctuations. In fact, for experimental biopolymers, the stretching and bending stiffness constants are not independent quantities. Rather, the ratio of the stretching and bending energy parameters,

$$\chi \equiv \frac{\gamma a^2}{4\kappa}, \tag{34}$$

presumably is rather constant and on the order of unity for real polymers, as in the case of an isotropic elastic cylinder.[36] Since higher values of the stretching parameter γ require a reduced simulation time step Δt (cf. beginning of this section), this is currently unfeasible for simulations including HI (the simulation time for a single hydrodynamic trajectories with 10^9 time steps lasting ~40 days on a standard single-core computer), we therefore continue our discussion with free-draining simulations. This restriction seems not to be serious, though, as the results in Fig. 10 showed that hydrodynamics are rather unimportant for the MSD of the scalar end-to-end distance anyways. In Fig. 12, we show the scalar end-to-end distance MSD from free-draining simulations, in which γ and κ where simultaneously modified keeping $\chi = 1.25$ constant. As is clearly seen, the trends observed in Fig. 10 remain unchanged: when increasing the ratio l_p/L, the local exponents gradually decrease (below 3/4), in qualitative agreement with the experimental data shown in Fig. 9.

We cautiously remark that experimentally, the ratio l_p/L is varied by choosing filaments of different contour lengths L while keeping the persistence length l_p fixed, while in our simulations the persistence length l_p is varied while keeping L fixed. These two scenarios are not strictly equivalent since an additional length scale, the monomer radius a, is present in the problem, giving a second dimensionless length-scale ratio L/a. In order to look into this, we in Fig. 13 show MFT results of the end-monomer and end-to-end vector MSDs for filaments of varying length to monomer radius ratio L/a, but constant ratio $l_p/L = 1$.

Note that the dependence on the monomer radius a can be scaled out in the free-draining limit; in other words,

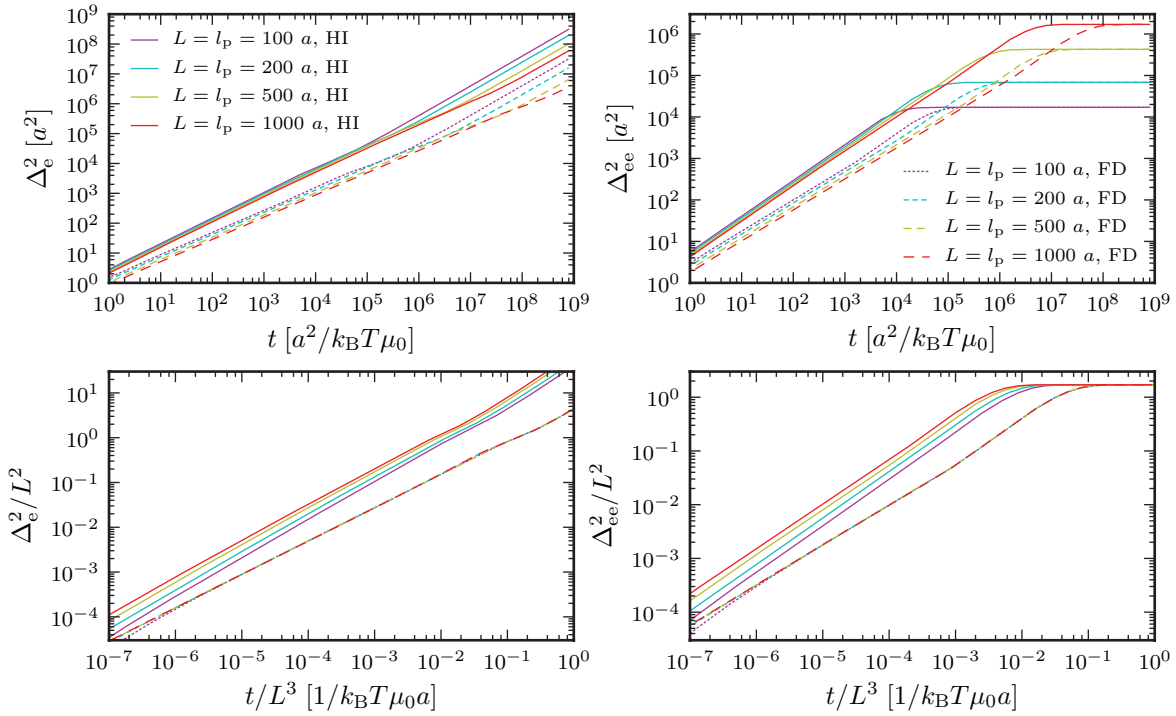

FIG. 13. (Upper left) MFT results for the end-monomer position vector MSD with hydrodynamic interactions (*solid lines*) and in the free-draining limit (FD, dashed lines) for filaments of varying contour length L and persistence length l_p, but constant ratio $l_p/L = 1$. (Lower left) A rescaling of time and MSD by the polymer length L yields a collapse of the free-draining MSDs on a master curve, deviations at small times resulting from differences in the mode-number cutoff N (cf. Sec. III B). Note that in the presence of HI no collapse is obtained. (Upper and lower right) Same plots for the end-to-end vector MSD.

free-draining relaxation dynamics are characterized by the ratio l_p/L only, as is clearly seen in the lower panels of Fig. 13, where we show the data rescaled by the polymer length L. On the other hand, HI give rise to a genuine logarithmic dependence of the dynamics on the ratio L/a. The dilemma is that our simulations do not span a large enough range of ratios l_p/L and L/a in order to extract the full scaling behavior, while the MFT cannot be used to calculate the experimentally measured scalar end-to-end distance MSD. Nevertheless, it is conceivable that the scaling in terms of one parameter only, namely, the ratio l_p/L, observed in the MFT for the MSDs of the vectorial observables without HI (Fig. 13), also holds for the scalar end-to-end distance MSD, for which the hydrodynamic effects have been shown to be rather unimportant in simulations (Fig. 10). This suggestion is enforced by the observation that experiments and simulation results for the scalar end-to-end distance MSD in Figs. 9 and 12 show similar behavior for matching values of l_p/L, although the values of L/a are very different. Based on the similar qualitative trends seen in the restricted experimental and simulation data sets displayed in Figs. 9 and 12, we are led to the following tentative conclusions: (i) local exponents for the scalar end-to-end distance MSD do not show characteristic plateau values but rather continuously decrease with increasing time and (ii) the dynamic scaling varies with polymer stiffness l_p/L, where values of $\alpha \gtrsim 3/4$ are observed for more flexible chains ($l_p/L < 1$), while exponents $\alpha \lesssim 3/4$ are characteristic for stiffer filaments ($l_p/L > 1$). These observations crucially depend on the presence of stretching fluctuations, as indeed experimentally present for elastic biopolymers. The strength of HI, which has sizeable effects on the MSDs of vectorial observables, mainly reduces to a temporal rescaling for the case of the scalar end-to-end distance MSD. Given these results, the collapse of experimental scalar end-to-end MSDs for different l_p/L on a single master-curve,[10] calls for further experimental investigations in light of the presence of stretching fluctuations as described by an extensible WLC model with finite χ.

V. CONCLUSIONS

In this paper we have presented results from hydrodynamic and free-draining BD simulations of a single semiflexible filament in the vicinity of a hydrodynamic no-slip wall: by varying the distance to the boundary, we could accurately resolve the influence of hydrodynamic screening on typical dynamic quantities, such as the end-monomer and end-to-end vector MSD of the polymer filament; the weakening of HI when approaching the wall is clearly reflected in these observables. Though being less accurate than in the three-dimensional case, the adaptation of a hydrodynamic mean field theory nicely captures the trends seen in the simulations: the slowing down of the overall dynamics and the crossover towards free-draining dynamic scaling when approaching the wall; in addition the theoretical approach allows to consider polymer lengths inaccessible in simulations due to the increased computational costs.

Our analysis reveals that (screened) hydrodynamics contribute differently to different dynamic variables: MSDs of vectorial quantities such as the end-monomer position and

the end-to-end vector show distinct plateaus in their local slopes, which are similar over a broad range of stiffnesses and gradually decrease when approaching the surface. Nevertheless, hydrodynamics continue to be important at polymer-wall separations on the order of the monomer-size; the free-draining limit therefore remains an inaccurate approximation to the actual dynamics, even very close to planar surfaces. To what extent similar reservations hold in other geometries or in non-dilute polymer solutions remains for future investigations.

On the other hand, rotations of the entire filament are factored out in the scalar end-to-end distance MSD, and the dynamic scaling exponent rather results from an interplay of stretching and bending stiffness; here, the role of hydrodynamic screening is mainly reduced to a temporal rescaling. The non-universal dependence of the scaling exponent on the persistence length to contour length ratio l_p/L seen in the free-draining simulations qualitatively agrees with a similar dependence seen in our reanalysis of experimental data for f-actin filaments[10] and crucially depends on the fact that one includes chain stretching fluctuations in the theoretical modeling as appropriate for elastic biopolymers.

On the basis of our findings, the characterization of previous experimental data in terms of a single dynamic scaling exponent appears oversimplified; experiments resolving more dynamic observables than the usual scalar end-to-end MSD, extending the analysis to a larger range of stiffnesses l_p/L, and rigorously identifying the hydrodynamic influence of nearby boundaries would certainly be helpful in shining more light on the rich and complex relaxation dynamics of single semiflexible polymers as well as of polymer networks.

ACKNOWLEDGMENTS

Financial support from the DFG (SFB 863) and the Elitenetzwerk Bayern in the framework of CompInt (YvH) is acknowledged.

APPENDIX: ROTNE-PRAGER LEVEL OF THE BLAKE TENSOR

1. Explicit entries of the tensor

As outlined in Sec. II, the Rotne-Prager level of the Blake tensor describing the approximate HI of finite sized particles near a no-slip wall at $z = 0$ is obtained from the Blake tensor $\overleftrightarrow{\boldsymbol{\mu}}^{\mathrm{B}}$ by the operation,

$$\overleftrightarrow{\boldsymbol{\mu}}^{\mathrm{RPB}}(\boldsymbol{r}_i,\boldsymbol{r}_j) = \left[\left(1+\frac{a^2}{6}\nabla_{\boldsymbol{r}}^2+\frac{a^2}{6}\nabla_{\boldsymbol{r}'}^2\right)\overleftrightarrow{\boldsymbol{\mu}}^{\mathrm{B}}(\boldsymbol{r},\boldsymbol{r}')\right]_{\boldsymbol{r}=\boldsymbol{r}_i,\boldsymbol{r}'=\boldsymbol{r}_j} = \overleftrightarrow{\boldsymbol{\mu}}^{\mathrm{RP}}(\boldsymbol{r}_i-\boldsymbol{r}_j)-\overleftrightarrow{\boldsymbol{\mu}}^{\mathrm{RP}}(\boldsymbol{r}_i-\bar{\boldsymbol{r}}_j)+\overleftrightarrow{\boldsymbol{\Delta\mu}}(\boldsymbol{r}_i,\boldsymbol{r}_j), \tag{A1}$$

where $\bar{\boldsymbol{r}}_j = (x_j, y_j, -z_j)^{\mathrm{T}}$ is the image position of particle j. In Eq. (A1), the definition of the Blake tensor (Eq. (2)) as well as of the RP tensor[20]

$$\overleftrightarrow{\boldsymbol{\mu}}^{\mathrm{RP}}(\boldsymbol{r}) = \frac{1}{8\pi\eta r}\left[\overleftrightarrow{\mathbf{1}}+\frac{\boldsymbol{r}\otimes\boldsymbol{r}}{r^2}\right]+\frac{a^2}{4\pi\eta r^3}\left[\frac{\overleftrightarrow{\mathbf{1}}}{3}-\frac{\boldsymbol{r}\otimes\boldsymbol{r}}{r^2}\right], \tag{A2}$$

were used. Compared to the case of an unbounded fluid, the hydrodynamic drag on bead i resulting from an external force acting on bead j is thus modified by two terms: the RP-interaction with the image of bead j [second term in Eq. (A1)] and the RP-level of the Stokes and source doublets [cf. Eqs. (4) and (5)] at the position of the image

$$\overleftrightarrow{\boldsymbol{\Delta\mu}}(\boldsymbol{r}_i,\boldsymbol{r}_j) \equiv \left[\left(1+\frac{a^2}{6}\nabla_{\boldsymbol{r}}^2+\frac{a^2}{6}\nabla_{\boldsymbol{r}'}^2\right)\left(\overleftrightarrow{\boldsymbol{\mu}}^{\mathrm{D}}(\boldsymbol{r}-\bar{\boldsymbol{r}}')-\overleftrightarrow{\boldsymbol{\mu}}^{\mathrm{SD}}(\boldsymbol{r}-\bar{\boldsymbol{r}}')\right)\right]_{\boldsymbol{r}=\boldsymbol{r}_i,\boldsymbol{r}'=\boldsymbol{r}_j}, \tag{A3}$$

for which we report the explicit entries. Note that our expressions differ from a previously reported version of the tensor.[37] The indices $\alpha \neq \beta \in \{x, y\}$ and z specify the entries of the matrix $\overleftrightarrow{\boldsymbol{\Delta\mu}}$, and the elements of the vectors $\boldsymbol{r}_i = (x_i, y_i, z_i)^T$, $\boldsymbol{r}_j = (x_j, y_j, z_j)^T$, and $\boldsymbol{R} = (R_x, R_y, R_z)^T$. The diagonal matrix entries are given by

$$\Delta\mu_{\alpha\alpha} = \frac{1}{4\pi\eta}\left(\frac{-z_i z_j}{R^3}\left(1-3\frac{R_\alpha^2}{R^2}\right)+\frac{a^2R_z^2}{R^5}\left(1-5\frac{R_\alpha^2}{R^2}\right)\right), \tag{A4}$$

$$\Delta\mu_{zz} = \frac{1}{4\pi\eta}\left(\frac{z_i z_j}{R^3}\left(1-3\frac{R_z^2}{R^2}\right)-\frac{a^2R_z^2}{R^5}\left(3-5\frac{R_z^2}{R^2}\right)\right), \tag{A5}$$

the off-diagonal ones read

$$\Delta\mu_{\alpha\beta} = \frac{1}{4\pi\eta}\left(\frac{3z_i z_j R_\alpha R_\beta}{R^5}-5a^2\frac{R_\alpha R_\beta R_z^2}{R^7}\right), \tag{A6}$$

$$\Delta\mu_{\alpha z} = \frac{1}{4\pi\eta}\left(\frac{z_j R_\alpha}{R^3}\left(1-3\frac{z_i R_z}{R^2}\right)-\frac{a^2R_\alpha R_z}{R^5}\left(2-5\frac{R_z^2}{R^2}\right)\right), \tag{A7}$$

$$\Delta\mu_{z\alpha} = \frac{1}{4\pi\eta}\left(\frac{z_j R_\alpha}{R^3}\left(1+3\frac{z_i R_z}{R^2}\right)-5\frac{a^2R_\alpha R_z^3}{R^7}\right). \tag{A8}$$

Altogether, HI described by Eqs. (A1)–(A8) are equivalent to the expressions in Ref. 19. Note the following typo in a previous publication by Kim and Netz:[18] in Eq. (2.14), the plus sign in front of the last line should be replaced by a minus sign in order to obtain the above expressions.

2. Preaveraged form of the hydrodynamic tensor

For the two-dimensional version of the MFT in Sec. III B, the 2×2-submatrix of $\overleftrightarrow{\boldsymbol{\mu}}^{\mathrm{RPB}}$ corresponding to the x- and y-coordinates is preaveraged by the help of the two-dimensional Gaussian probability distribution given in Eq. (26). The

right-hand side of Eq. (25) yields

$$\mu_{\text{avg}}^{\text{RPB}}/\mu_0 = \frac{\sqrt{\pi}(9\sigma+4)\text{erfc}\left(\frac{2}{\sqrt{\sigma}}\right)}{8\sigma^{3/2}} - \frac{e^{-4/\sigma}}{4\sigma} + \frac{e^{-4/\sigma}}{4\sigma^3\left(z^2+1\right)^{5/2}}$$
$$\times(\sigma^2+\sigma(7\sigma+32)z^2+(15\sigma^2+80\sigma+64)z^4$$
$$+2(3\sigma^2+36\sigma+64)z^6+8(3\sigma+8)z^8) - \frac{\sqrt{\pi}}{8\sigma^{7/2}}$$
$$\times e^{\frac{4z^2}{\sigma}}(32(3\sigma+8)z^4+4\sigma(9\sigma+32)z^2$$
$$+\sigma^2(9\sigma+4))\text{erfc}\left(2\sqrt{\frac{z^2+1}{\sigma}}\right), \quad \text{(A9)}$$

where the mean squared distance between s and s' [Eq. (26)] is denoted by $\sigma \equiv \sigma(|s-s'|)$, and where for convenience we have set $a = 1$. Note, that the positive exponential in the penultimate line of Eq. (A9) is a source of numerical error for values $z \gtrsim 25\,a$ when using double precision numbers; in this case an asymptotic expansion of the above expression for the limit $z \to \infty$ can be used instead.

[1] O. B. Usta, J. E. Butler, and A. J. C. Ladd, Phys. Rev. Lett. **98**, 098301 (2007).
[2] L. Cannavacciuolo, R. G. Winkler, and G. Gompper, Europhys. Lett. **83**, 34007 (2008).
[3] N. Hoda and S. Kumar, Phys. Rev. E **79**, 020801(R) (2009).
[4] M. Hinczewski, X. Schlagberger, M. Rubinstein, O. Krichevsky, and R. R. Netz, Macromolecules **42**, 860 (2009).
[5] M. Hinczewski and R. R. Netz, Europhys. Lett. **88**, 18001 (2009).
[6] M. Hinczewski and R. R. Netz, Physica A **389**, 2993 (2010).
[7] R. Chelakkot, R. G. Winkler, and G. Gompper, Europhys. Lett. **91**, 14001 (2010).
[8] D. J. Bonthuis, C. Meyer, D. Stein, and C. Dekker, Phys. Rev. Lett. **101**, 108303 (2008).
[9] J. Tang, S. L. Levy, D. W. Trahan, J. J. Jones, H. G. Craighead, and P. S. Doyle, Macromolecules **43**, 7368 (2010).
[10] L. Le Goff, O. Hallatschek, E. Frey, and F. Amblard, Phys. Rev. Lett. **89**, 258101 (2002).
[11] R. Shusterman, S. Alon, T. Gavrinyov, and O. Krichevsky, Phys. Rev. Lett. **92**, 048303 (2004).
[12] E. P. Petrov, T. Ohrt, R. G. Winkler, and P. Schwille, Phys. Rev. Lett. **97**, 258101 (2006).
[13] R. Granek, J. Phys. II **7**, 1761 (1997).
[14] C. Sendner and R. R. Netz, Europhys. Lett. **79**, 58004 (2007).
[15] C. Sendner and R. R. Netz, Europhys. Lett. **81**, 54006 (2008).
[16] T. Ando and J. Skolnick, Proc. Natl. Acad. Sci. U.S.A. **107**, 18457 (2010).
[17] J. R. Blake, Proc. Cambridge Philos. Soc. **70**, 303 (1971).
[18] Y. W. Kim and R. R. Netz, J. Chem. Phys. **124**, 114709 (2006).
[19] N. Hoda and S. Kumar, J. Chem. Phys. **127**, 234902 (2007).
[20] J. Rotne and S. Prager, J. Chem. Phys. **50**, 4831 (1969).
[21] M. D. Carbajal-Tinoco, R. Lopez-Fernandez, and J. L. Arauz-Lara, Phys. Rev. Lett. **99**, 138303 (2007).
[22] G. S. Perkins and R. B. Jones, Physica A **189**, 447 (1992).
[23] M. Stimson and G. B. Jeffery, Proc. R. Soc. London, Ser. A **111**, 110 (1926).
[24] J. Happel and H. Brenner, *Low Reynolds Number Hydrodynamics* (Noordhoff, Leyden, 1973).
[25] D. L. Ermak and J. A. McCammon, J. Chem. Phys. **69**, 1352 (1978).
[26] M. Doi and S. F. Edwards, *The Theory of Polymer Dynamics* (Oxford University Press, New York, 1988).
[27] Y. von Hansen, R. R. Netz, and M. Hinczewski, J. Chem. Phys. **132**, 135103 (2010).
[28] O. Kratky and G. Porod, Rec. Trav. Chim. Pays-Bas **68**, 1106 (1949).
[29] R. G. Winkler, P. Reineker, and L. Harnau, J. Chem. Phys. **101**, 8119 (1994).
[30] B. Y. Ha and D. Thirumalai, J. Chem. Phys. **103**, 9408 (1995).
[31] R. G. Winkler, J. Chem. Phys. **127**, 054904 (2007).
[32] L. Harnau, R. G. Winkler, and P. Reineker, J. Chem. Phys. **104**, 6355 (1996).
[33] B. H. Zimm, J. Chem. Phys. **24**, 269 (1956).
[34] E. H. Stanley, *Introduction to Phase Transitions and Critical Phenomena* (Oxford University Press, New York, 1987).
[35] P. E. Rouse, J. Chem. Phys. **21**, 1272 (1953).
[36] M. Manghi, X. Schlagberger, Y. W. Kim, and R. R. Netz, Soft Matter **2**, 653 (2006).
[37] E. M. Gauger, M. T. Downton, and H. Stark, Eur. Phys. J. E **28**, 231 (2009).